Resource

Cell Chemical Biology

Multicolor Electron Microscopy for Simultaneous Visualization of Multiple Molecular Species

Graphical Abstract

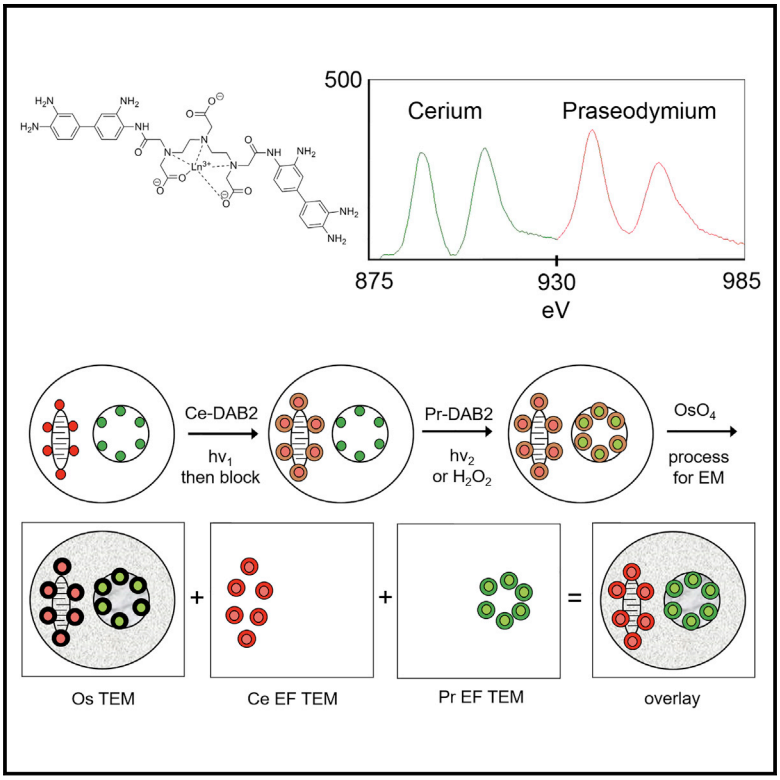

Highlights

- Multicolor EM paints multiple cellular markers by locally depositing specific Ln^{3+}
- Each Ln^{3+} visualized by electron energy-loss spectroscopy and energy-filtered EM
- Elemental maps overlaid on conventional EM give multicolor EM
- Applicable to immuno, genetically encoded and molecular probes in cells and tissue

Authors

Stephen R. Adams, Mason R. Mackey, Ranjan Ramachandra, ..., Ben N.G. Giepmans, Mark H. Ellisman, Roger Y. Tsien

Correspondence

sadams@ucsd.edu

In Brief

Multicolor electron microscopy (EM) is introduced by Adams et al. for imaging multiple, specific cellular components by locally depositing lanthanides and using electron energy-loss spectroscopy and energy-filtered EM. Analogous to multicolor fluorescence this method offers full spatial resolution of EM.

Adams et al., 2016, Cell Chemical Biology *23*, 1417–1427
November 17, 2016 © 2016 Elsevier Ltd.
http://dx.doi.org/10.1016/j.chembiol.2016.10.006

CellPress

Please cite this article as: Adams et al., Multicolor Electron Microscopy for Simultaneous Visualization of Multiple Molecular Species, Cell Chemical Biology (2016), http://dx.doi.org/10.1016/j.chembiol.2016.10.006

Cell Chemical Biology
Resource

Multicolor Electron Microscopy for Simultaneous Visualization of Multiple Molecular Species

Stephen R. Adams,[1,9,*] Mason R. Mackey,[2] Ranjan Ramachandra,[2] Sakina F. Palida Lemieux,[1] Paul Steinbach,[3] Eric A. Bushong,[2] Margaret T. Butko,[1,6] Ben N.G. Giepmans,[2,7] Mark H. Ellisman,[2,4] and Roger Y. Tsien[1,3,5,8]
[1]Department of Pharmacology
[2]National Center for Microscopy and Imaging Research
[3]Howard Hughes Medical Institute
[4]Department of Neurosciences
[5]Department of Chemistry & Biochemistry
University of California, San Diego, La Jolla, CA 92093, USA
[6]Present address: Biodesy Inc, 384 Oyster Point Boulevard Suite #8, South San Francisco, CA 94080, USA
[7]Present address: Department of Cell Biology, University Medical Center Groningen, A. Deusinglaan 1, 9713 AV Groningen, the Netherlands
[8]Deceased August 24, 2016
[9]Lead Contact
*Correspondence: sadams@ucsd.edu
http://dx.doi.org/10.1016/j.chembiol.2016.10.006

SUMMARY

Electron microscopy (EM) remains the primary method for imaging cellular and tissue ultrastructure, although simultaneous localization of multiple specific molecules continues to be a challenge for EM. We present a method for obtaining multicolor EM views of multiple subcellular components. The method uses sequential, localized deposition of different lanthanides by photosensitizers, small-molecule probes, or peroxidases. Detailed view of biological structures is created by overlaying conventional electron micrographs with pseudocolor lanthanide elemental maps derived from distinctive electron energy-loss spectra of each lanthanide deposit via energy-filtered transmission electron microscopy. This results in multicolor EM images analogous to multicolor fluorescence but with the benefit of the full spatial resolution of EM. We illustrate the power of this methodology by visualizing hippocampal astrocytes to show that processes from two astrocytes can share a single synapse. We also show that polyarginine-based cell-penetrating peptides enter the cell via endocytosis, and that newly synthesized PKMζ in cultured neurons preferentially localize to the postsynaptic membrane.

INTRODUCTION

Electron microscopy (EM) of biological samples remains the ultimate method for imaging cellular ultrastructure despite the recent advances in super-resolution microscopy (Betzig et al., 2006; Hell, 2007; Huang et al., 2009). Contrast in standard EM of epoxy-embedded samples is dependent upon the deposition of heavy metals such as osmium, uranium, or lead to highlight cellular components including protein, lipid, or nucleic acid using long-established and poorly selective stains. Selective visualization of specific proteins or macromolecules can be achieved using antibodies conjugated to gold particles or quantum dots of distinctive size, but poor penetrability of such labels in fixed cells or tissues limits the use of optimal fixation methods that preserve ultrastructure (Schnell et al., 2012). This limitation can be avoided by the in situ oxidation of diaminobenzidine (DAB) generating a localized osmiophilic precipitate by photosensitizing dyes conjugated to antibodies or ligands (Deerinck et al., 1994; Maranto, 1982), genetically targeted biarsenicals (Gaietta et al., 2002) and genetically encoded chimeras of miniSOG (Shu et al., 2011). Peroxidases (such as horseradish peroxidase, HRP) also generate similar precipitates from DAB on treatment with hydrogen peroxide (H_2O_2) and robust genetically encoded versions have been developed recently (Kuipers et al., 2015; Lam et al., 2015; Martell et al., 2012). The high penetrability of small dyes, DAB, and oxygen or H_2O_2 into optimally fixed cells or tissues enables specific labeling with preservation of cellular ultrastructure. The target protein becomes negatively stained by the surrounding oxidized DAB precipitate, which may not be readily distinguishable from heavy staining from endogenous cellular structures such as membranes and the postsynaptic density.

In this work, we demonstrate a method (Figure 1A) that can differentiate the DAB precipitate from the general staining of endogenous cellular material and permits identification and imaging of successively deposited DAB, each at a targeted or specified protein or cellular target. By precipitating DAB conjugated to lanthanide chelates rather than DAB itself, a specific metal such as Ce^{3+} is locally deposited. After washing out the unreacted DAB-chelator-Ln, a further round of deposition of DAB-chelator bound to another lanthanide ion such as Pr^{3+} is carried out by photooxidation of a second photosensitizer targeted to another cellular site or protein, at wavelengths that do not excite the first fluorophore. Alternatively, peroxidases can be used to generate the second precipitate. Following conventional postfixation staining with osmium tetroxide and electron microscopy of sections from embedded samples, the two

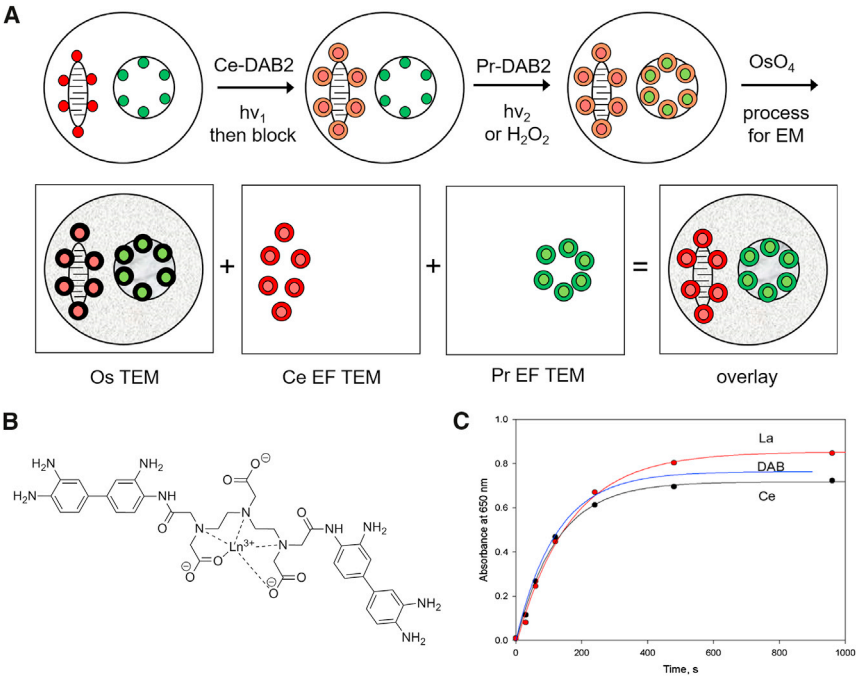

Figure 1. Two-Color EM using EELS and EFTEM

(A) Scheme of the process applied to cells with stained mitochondrial (red) and nuclear membranes (green) are first selectively irradiated to photooxidize the red photosensitizer and precipitate Ce-DAB2 (brown ring). After washing and replacement with Pr-DAB2, illumination at an orthogonal wavelength generates a precipitate at the nuclear membrane. Alternatively, the Pr-DAB2 can be oxidized by hydrogen peroxide following immunoperoxidase labeling. Following conventional osmification (black ring), embedding, sectioning, and TEM, EFTEM yields pseudocolored elemental maps for Ce and Pr that are overlaid on the conventional osmium image.

(B and C) Structure of Ln-DAB2 (B) and La- and Ce-DAB2 (C) are precipitated at a similar rate to DAB by photosensitization of eosin.

precipitates containing different tightly bound lanthanide ions can be spectrally separated using spatially resolved electron energy-loss spectroscopy (EELS), which is implemented by energy-filtered transmission electron microscopy (EFTEM). Elemental distribution maps for the two metals obtained by EFTEM reveal their spatial distribution, and can be overlaid as pseudocolors on the conventional black and white electron micrograph to give a multicolor image superimposed on the cellular ultrastructure. The method is also useful for only a single deposited lanthanide, because the EELS signal is not obscured by staining of endogenous cellular structures by osmium or other heavy metals used for contrast in EM.

RESULTS

Synthesis of DAB-Metal Chelate Conjugates

In designing metals complexed to DAB that would precipitate on oxidation, we considered the following requirements. The metal ions should have strong, distinct EELS peaks that are simultaneously quantifiable, and must form high-affinity chelates to prevent any loss of metal ions during DAB oxidation and subsequent processing leading to a decreased EELS signal or a false-positive signal. The lanthanide series have a similar charge (3+), ionic radii, and suitable EELS signals and should bind to a conjugate of diethylenetriamine-pentaacetic acid (DTPA) with two DAB (Figure 1B) and with three carboxylates to form a high-affinity complex (dissociation constants of 0.1–1 fM for Gd^{3+} have been reported for related DTPA-bisanilides) (Geze et al., 1996) with an overall neutral charge to facilitate precipitation. The DTPA-DAB_2 was synthesized by the reaction of DTPA anhydride with a five-fold excess of DAB to hinder the formation of polymers (Figure S1). Following removal of most of the unreacted DAB by extraction, the product DTPA-DAB_2 was precipitated. This solid was used for all subsequent photooxidation experiments with DTPA-DAB_2 despite containing some unreacted DAB and monomer DTPA-DAB as measured and quantified by liquid chromatography-mass spectrometry (LC-MS) (Figure S2). When free DAB was removed from the material by high-performance liquid chromatography (HPLC), the purified DTPA-DAB_2 generated less precipitate in cuvette experiments and failed to generate the expected localized precipitate in cells (data not shown).

Metal Binding to Lanthanides and Precipitation of Metal Complex on Oxidation

The complexation of DTPA-DAB_2 to lanthanide ions, Ln^{3+}, was measured by titration using arsenazo III as a colorimetric indicator to the endpoint and by comparison with an equal concentration of DTPA. Each batch synthesized gave between 75% and 85% purity by weight from titration, assuming the expected 1:1 stoichiometry, and closely matched the percent purity of DTPA-DAB_2 measured by HPLC (Figure S2). Precipitation of this so formed Ln DTPA-DAB_2 (Ln-DAB2) following photooxidation by photosensitization of eosin at 480 nm was measured by monitoring the absorbance from increasing scattering at 650 nm (Deerinck et al., 1994; Natera et al., 2011). Typical time courses for La-, Ce-, Pr-, Nd-, and Sm-DAB2 were similar to that of DAB (Figure 1C) and were in contrast to greatly decreased precipitate when no lanthanide was present, confirming the requirement of charge neutralization for efficient precipitation (data not shown). All the Ln-DAB2 tested showed limited solubility in 100 mM sodium cacodylate, pH 7.4, the buffer conventionally used for photooxidation in fixed cells and tissues and optimal for preserving ultrastructure in EM. To achieve a concentration close to the 2.5 mM value typically used for DAB, 2.5% dimethylformamide (DMF) was added as a co-solvent and the cacodylate buffer concentration was decreased to 50 mM. The final metal ion concentrations following filtration were determined by inductively coupled plasma mass spectroscopy to be about 0.8 mM with about 2 mM total DAB content (DTPA-DAB_2 and DAB) as measured by absorbance at 309 nm using an extinction coefficient of 14,200 M^{-1} cm^{-1}.

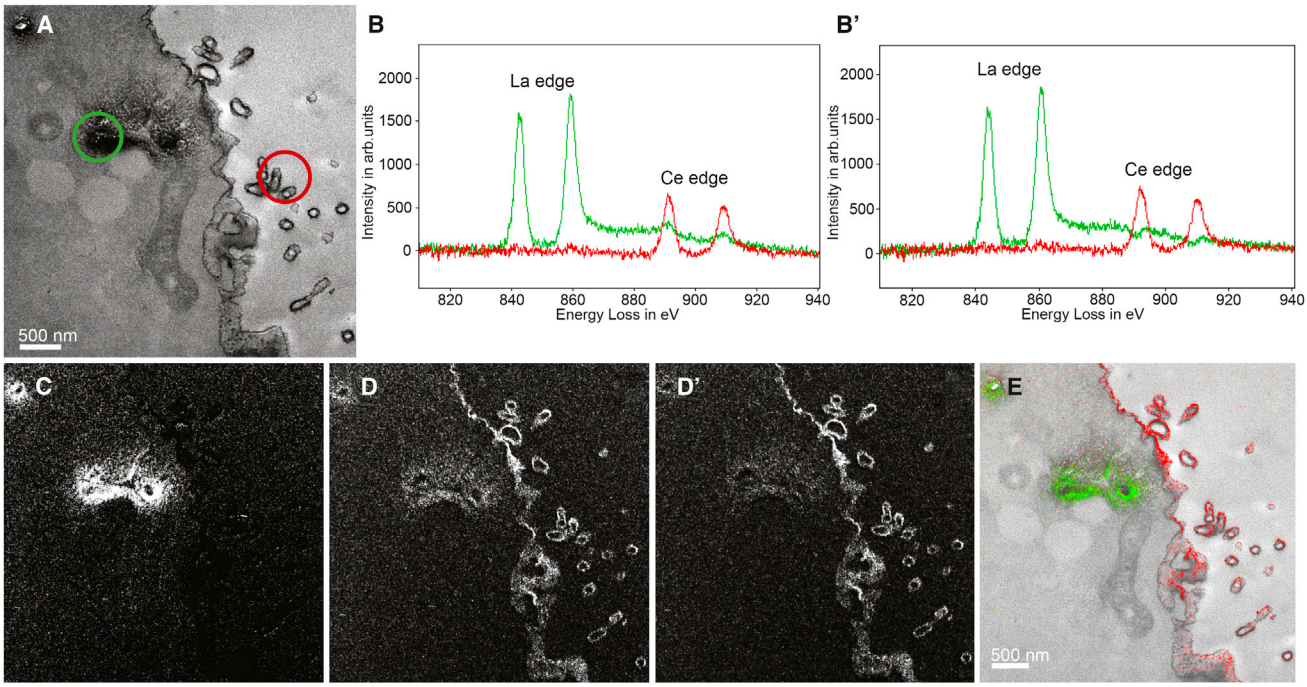

Figure 2. Two-Color EM of Golgi and Plasma Membrane in Tissue Culture Cells

(A) Conventional TEM image (1.4 nm/pixel) of an MDCK cell following photooxidation with La-DAB2 by NBD-ceramide-labeled Golgi and subsequent oxidation of Ce-DAB2 on the plasma membrane (PM) with HRP-labeled antibody to EPCAM.

(B) Spectra obtained at the Golgi region (green spectra) and at the PM containing EPCAM (red spectra); the respective regions are shown as circles in (A). The Golgi region shows a strong La signal with a weak Ce signal, the PM region shows only Ce. (B′) The cross-talk in the spectra shown in (B), due to Ce-DAB2 attaching to regions labeled with La-DAB2, has been mathematically subtracted.

(C and D) La and Ce elemental map obtained by the five-window method on the CCD (bin by four pixels, pixel size 4.4 nm), each energy window image was a sum of nine individual drift-corrected images, each acquired for a 60 s exposure. A Gaussian smoothing of blur radius 1 was applied to the images. (D′) The Ce map shown in (D), mathematically corrected to remove the cross-talk due to Ce-DAB2 attaching to regions labeled with La-DAB2.

(E) Two-color merge of the elemental maps (La in green and Ce in red), overlaid on the conventional TEM image.

Two-Color EM of Tissue Culture Cells

We next tested whether two Ln-DAB2 could be orthogonally precipitated in cells and whether the specific EELS signals of the two metals could be detected and separated as elemental images. Madine-Darby canine kidney (MDCK) cells stably expressing GFP fused to an epithelial cell adhesion molecule (GFP-EPCAM), were initially stained with NBD-ceramide, a Golgi-selective fluorescent probe capable of photosensitizing DAB (Pagano et al., 1991; Pagano et al., 1989; Takizawa et al., 1993), and then subsequently an antibody to the cell surface marker, EPCAM (Schnell et al., 2013), followed by a biotinylated secondary antibody. Following mild fixation, irradiation at 480 nm in the presence of La-DAB2 and oxygen gave faint darkening from formation of reaction product in cell regions corresponding to the fluorescence image of NBD-ceramide. The cells were treated with acetic anhydride to block any unreacted amines of the DAB moiety of the reaction product to prevent further reaction of the deposited precipitate. Ce-DAB2 was then precipitated after further labeling of EPCAM sites by HRP-streptavidin and incubation with hydrogen peroxide. Following osmification, resin embedding, and sectioning, a low-magnification unfiltered electron micrograph (Figure 2A) of a typical cell reveals the expected intracellular and plasma membrane staining from deposited precipitates at the Golgi and cell surface. However, EELS of regions at the Golgi or plasma membrane (circled in Figure 2A) revealed characteristic peaks from predominately La or Ce, respectively (Figure 2B). The small contaminating Ce signal at the Golgi probably resulted from unwanted deposition of Ce-DAB2 at the site of previously photooxidized Ln-DAB2 despite acetylation of any residual free amines, and could be mathematically subtracted in the EELS spectra (Figure 2B′), and the elemental maps for La and Ce (Figures 2C, 2D, and 2D′). To do this we selected a region in the field being observed that was expected to only contain La, such as the Golgi, and integrated the La and Ce peaks of the EELS spectrum in this area to give the fraction of contaminating Ce in the La channel, which was then subtracted from the La elemental map. These core-loss elemental maps were generated by subtraction of four images (two pre-edge and two after-peak images, see Experimental Procedures for details) rather than two with the traditional three-window method (Egerton, 1996), to minimize any effects of signal bleed-through of the lanthanides resulting from inaccurate background extrapolation. To reduce sample warping and drift, we found that taking multiple short-image acquisitions and carbon coating the sample were greatly beneficial. This five-window method shows a distinct signal from the appropriate cell regions with La at the Golgi and Ce at the plasma membrane.

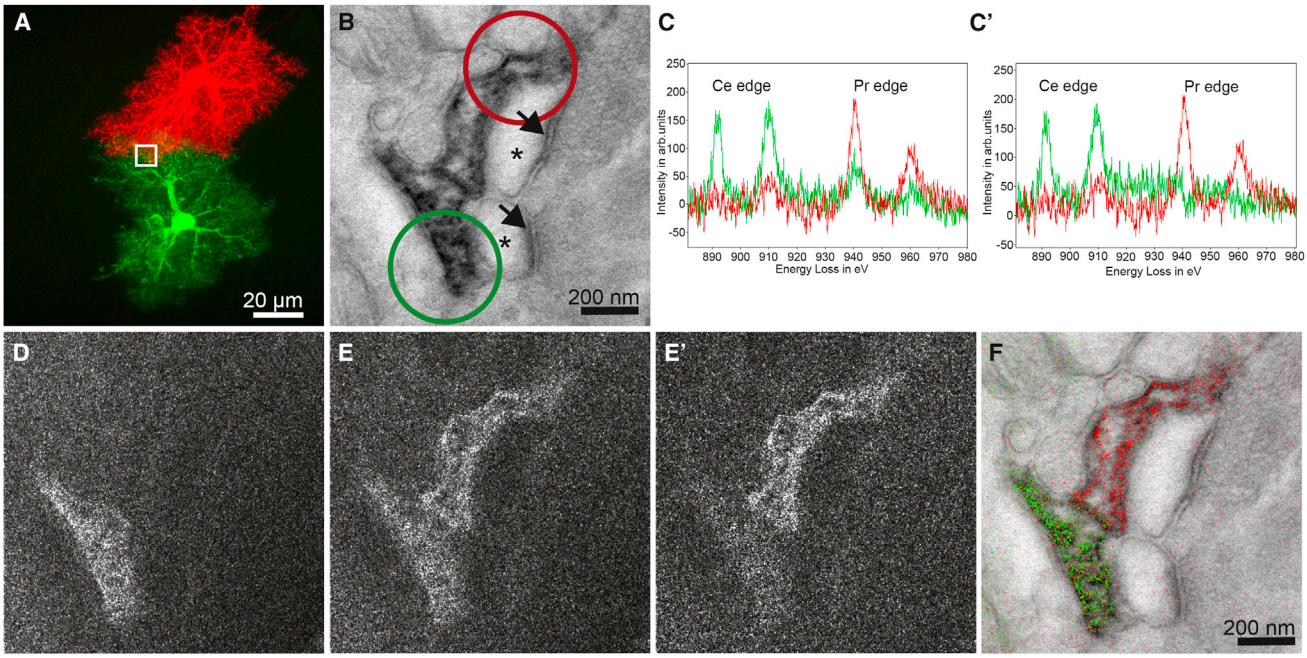

Figure 3. Two-Color EM of Hippocampal Astrocytes in Brain Slices

(A) Correlative fluorescent image of adjacent hippocampal astrocytes injected with lucifer yellow or neurobiotin/Alexa 568. The white box is the approximate region of the EM acquisition, shown in the following panels.

(B) Conventional TEM image (0.56 nm/pixel) showing astrocyte processes containing precipitated Ce- and Pr-DAB2 complexes contacting two spines synapsing (asterisk) with a bouton (postsynaptic densities indicated with arrows).

(C) EELS spectra obtained at the lower astrocyte (green spectra) photooxidized with Ce-DAB2 and upper astrocyte (red spectra) HRP enzymatically reacted Pr-DAB2; the respective regions are shown as circles in (B). The upper astrocyte contains predominately Pr, whereas the bottom has Pr and Ce signals. (C′) The cross-talk in the spectra shown in (C), due to Pr-DAB2 attaching to regions labeled with Ce-DAB2, has been mathematically subtracted.

(D and E) Ce and Pr elemental maps acquired on DE-12 detector (pixel size 0.42 nm; five-window method using a sum of 19 drift-corrected 50 s exposures per window, smoothed with Gaussian blur radius 3). (E′) Corrected Pr map, removing Pr-DAB from regions with Ce-DAB.

(F) Two-color merge of the spectrally separated elemental maps (green for Ce and red for Pr) overlaid on a conventional image, showing the two different astrocyte processes contacting the same synapse.

How should the two energy-filtered lanthanide maps and conventional transmission EM (TEM) be visually combined? We first tried "mixing," in Photoshop, the conventional TEM in grayscale (normal or inverted) with the lanthanide maps in red and green, respectively. However, the grayscale image tended to drown out the color images because the black pixels stayed black regardless of any colors mixed in (Figures S3A–S3E). Next we tried displaying the conventional TEM in blue, so that a region with strong La-DAB2 or Ce-DAB2 would appear cyan or magenta, respectively (Figures S3F and S3G). Unfortunately, regions with conventional TEM only tend to suffer because of the low psychophysical visibility of the blue channel. Assigning green to the conventional TEM and blue to the Ce-DAB2 deemphasized the latter too much and merely shifted the problem. Finally, we realized that the conventional TEM image has high spatial frequencies, resolution, and signal-to-noise, analogous to the luminance channel in television, whereas the colors should be displayed as lower-resolution overlays, effectively modulating the alpha channel for transparency versus opacity. Therefore, we used a custom algorithm to generate pseudocolored overlays of the La and Ce elemental maps on the monochrome unfiltered osmium image (conventional EM image) to yield a two-hue representation of marker distribution with the resolution of an electron micrograph (Figures 2E and S3H). An advantage of this algorithm is that it can be generalized to three or more pseudocolor channels.

Hippocampal Astrocyte Cell Tracing in Brain Slices

Following this proof of principle, we tested the application of this method to biological questions that required the ultrastructural resolution of EM and labeling of two cell markers. Protoplasmic astrocytes in the mouse hippocampus establish distinct territories with limited overlap between peripheral processes. These fine peripheral processes intimately contact and modulate neuronal synapses (Haydon, 2001; Haydon and Carmignoto, 2006). Whether synapses located at domain boundaries are shared by two astrocytes is unknown because both synaptic profiles and the fine astrocytic processes near synapses are generally beyond the resolution limit of light microscopy (Bushong et al., 2004; Bushong et al., 2002; Halassa et al., 2007). We injected two adjacent astrocytes in fixed hippocampal slices with either lucifer yellow or a combination of Alexa 568 and neurobiotin (Figure 3A). Ce-DAB2 was photooxidized by lucifer yellow at 470 nm. Acetylimidazole was used to passivate the Ce-DAB2 precipitate instead of acetic anhydride because of its greater stability at neutral pH, higher solubility in water, and

self-buffering at pH 5, which favors reaction with the aromatic amines of DAB (Oakenfull and Jencks, 1971). Then neurobiotin was captured with HRP-streptavidin, which in turn was reacted with Pr-DAB2 and H_2O_2. After osmification and embedding in resin, sections were examined by EM for synapses with surrounding densely stained astrocyte processes containing both Ce and Pr signals by EELS. An example of a perforated synapse with clearly defined synaptic cleft and pre- and postsynaptic components marked by synaptic vesicles and postsynaptic densities, respectively, is shown in Figure 3B. EELS of sub-regions of each of the two astrocytic processes contacting the synapse revealed predominately Ce or Pr signals (Figure 3C). Some signal from Pr is still present in the Ce astrocyte, perhaps from incomplete inactivation of the first Ce-DAB2 precipitate by limited penetration of the acetylimidazole into the fixed brain slice. The individual elemental maps (Figures 3D and 3E, and corrected Pr map, 3E′) and their overlay with an unfiltered EM (Figure 3F) also indicate that the processes from two astrocytes can share a single synapse.

Endosomal Uptake of Cell-Penetrating Peptides

We next explored whether it is feasible to precipitate Ce- and Pr-DAB by successive irradiation of two spectrally distinct photosensitizers rather than photooxidation followed by HRP-mediated oxidation. We first generated a Ce-DAB2 precipitate by 480 nm irradiation of nuclear targeted miniSOG (Shu et al., 2011) and then tested the ability of ReAsH-labeled tetracysteine-tagged connexin 43 that form gap junctional plaques (Gaietta et al., 2002) to photooxidize DAB2 when excited at 560 nm. Pr-DAB2 was precipitated as expected at the plasma membrane but also in the nucleus suggesting that the initial precipitate itself could act as a photosensitizer of DAB (data not shown). Ce-DAB2 photooxidized in a cuvette shows a broad absorbance centered at 500 nm that extends to 600 nm, and correspondingly in cells we found that after nuclear deposition of Ce-DAB2 by miniSOG at 480 nm, irradiation at >630 nm would not precipitate Pr-DAB2. ReAsH does not absorb at 630 nm, so we tested the ability of far-red photosensitizers such as the phthalocyanine dye, IRDye 700DX (Mitsunaga et al., 2011; Peng et al., 2006), to photooxidize Pr-DAB2.

Cell-penetrating peptides (CPP), including oligomers of cationic amino acids such as arginine (n = 9–14), have been extensively used to deliver membrane-impermeant molecules or particles into the cytoplasm of cells (Copolovici et al., 2014). CPPs rapidly bind to the plasma membrane and are hypothesized to enter cells via endocytosis (Brock, 2014; Kaplan et al., 2005; Richard et al., 2003). To determine whether polyarginine CPPs enter cells via the endocytic pathway, we examined the localization of an internalized Arg_{10} peptide compared with RAB5A, a small GTPase that localizes to endosomal membranes, at a scale too small to resolve using conventional light microscopy. We incubated HeLa cells expressing RAB5A fused to miniSOG (Shu et al., 2011) with an Arg_{10} peptide conjugated to an IRDye 700DX photosensitizer (Figure S4) that can polymerize DAB. After the cells were incubated with Arg_{10}-IRDye 700DX peptide for 2 hr, they were fixed and imaged by light microscopy (Figure 4). We detected bright intracellular puncta from the endocytosed Arg_{10}-IRDye 700DX peptide (Figure 4C) that partially co-localized with miniSOG fluorescence (Figures 4B and 4D). We then irradiated the sample at 480 nm to photooxidize Ce-DAB2 catalyzed by miniSOG, removed unreacted Ce-DAB2 by washing, blocked amines with acetylimidazole, and then illuminated it at 680 nm to photooxidize Pr-DAB2 catalyzed by IRDye 700DX. Both endosomes and multivesicular bodies (MVB) were photooxidized and visible in the unfiltered EM and both contain precipitated Ce and Pr by EELS (Figures 4E and 4I, respectively). The elemental maps and overlay with conventional EM image (Figures 4F–4H) indicate that Ce is concentrated on the endosome periphery in accordance with the expected cytoplasmic localization of RAB5A, whereas Pr is predominately in the endosome lumen. In this example, we could not correct the Ce channel for contaminating Pr as EELS spectra with adequate signal-to-noise could not be obtained solely for endosomal lumen or the periphery. The corresponding images of MVB (Figures 4J–4L) also show a similar distribution of Ce and Pr but with less cytosolic Ce, and several densely Ce-stained luminal vesicles formed by inward budding of the endosomal membrane. Endosomal localization of RAB5A has been shown to progressively decrease during early endosome maturation to MVB (Rink et al., 2005) which is in agreement with our results. In addition, Arg_{10}-IRDye 700DX colocalization with RAB5A in intracellular vesicles confirms that polyarginine-based CPPs enter the cell via endocytosis.

Tracking Newly Synthesized PKMζ in Cultured Neurons

Finally, we used EELS analysis of a single lanthanide-conjugated DAB to confirm DAB-based labeling that is not readily distinguishable from background with conventional TEM, particularly in regions that are normally electron dense such as the neuronal postsynaptic density. The kinase PKMζ has been implicated in long-term memory maintenance and is upregulated following neuronal activity (Shao et al., 2012), but the function and precise sub-synaptic localization of these new PKMζ copies is unclear. We fused PKMζ cDNA to a TimeSTAMP reporter, TS:YSOG3 (Palida et al., 2015), that contains both YFP and miniSOG and allows newly synthesized proteins to be labeled in a drug-dependent manner using the small-molecule BILN-2061. New copies can be visualized by correlated light and EM in a manner similar to previous TimeSTAMP reporters incorporating a split YFP and miniSOG (Butko et al., 2012) (Figure S5). We induced chemical long-term potentiation by stimulating TS:YSOG3-PKMζ-transfected rat neurons in culture with forskolin and rolipram and then immediately added BILN-2061 for 24 hr to label newly synthesized copies of PKMζ. These new copies were visible by YFP fluorescence and then were illuminated so that miniSOG would catalyze photooxidation of Ce-DAB2. After osmification, darkening was visible throughout the neuron at low magnification (Figure 5A) and labeling appeared at postsynaptic membranes in TEM (Figure 5B), yet it was unclear whether this signal was derived from DAB deposition or endogenous synaptic electron density. To confirm that the apparent signal was representative of newly produced PKMζ protein, we used EELS to visualize Ce at the same synapse. We found that the Ce signal was enhanced at the postsynaptic membrane (Figures 5C and 5D at lower magnification, E and F at higher magnification) confirming that new copies of PKMζ preferentially localize to the postsynaptic membrane, consistent with previous reports for PKMζ localization (Hernández et al., 2014). Unstimulated neurons that

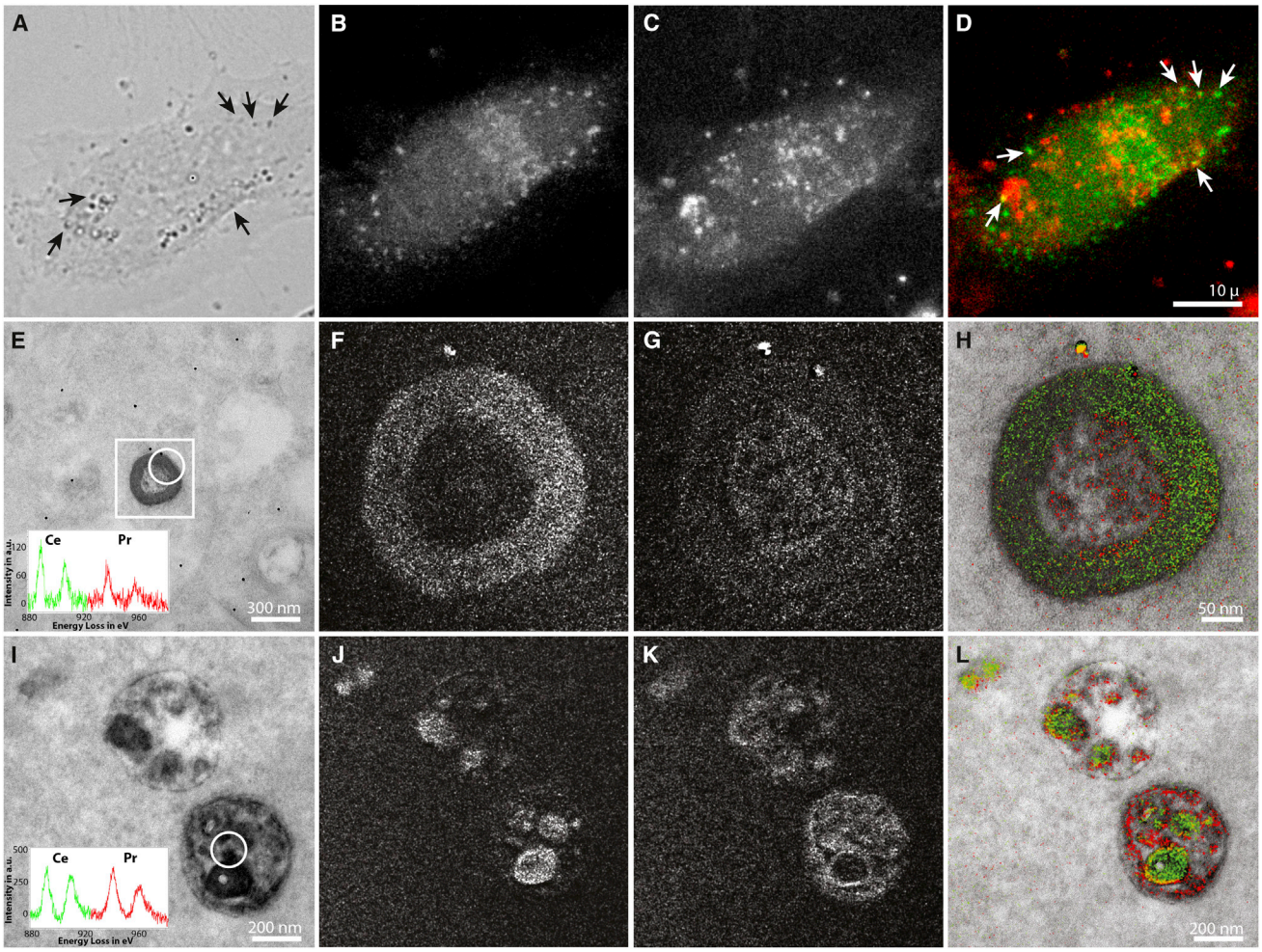

Figure 4. Two-Color EM of Endosomal Uptake of CPPs

(A–D) Transmitted light image of miniSOG-RAB5A transfected HEK293 cell treated with Arg_{10}-IRDye 700DX showing endosomes (arrows) following photooxidation (A). Corresponding fluorescent images of (B) miniSOG-RAB5A, (C) Arg_{10}-IRDye 700DX labeling, and (D) two-color overlay of fluorescent images with typical endosomes arrowed.

(E) Conventional TEM image (0.45 nm/pixel) of an endosome after consecutive photooxidization of Ce-(miniSOG-RAB5A) and Pr-DAB2 (Arg_{10}-IRDye 700DX). The inset is the EELS spectrum from the circled region and the rectangular box is the region of elemental map acquisitions, shown in the subsequent panels.

(F and G) Ce and Pr elemental maps acquired on DE-12 detector, respectively, of the endosome (0.2 nm/pixel; five-window method using a sum of 12 drift-corrected 50 s exposure per window, smoothed with Gaussian blur radius 3).

(H) Two-color merge of the Ce (green) and Pr (red) elemental maps overlaid on the TEM image reveals that the Arg_{10} is lumenal and RAB5A is on the cytoplasmic face of the endosome.

(I) TEM image (0.45 nm/pixel) of an MVB from the same cell with the EELS spectrum of the circled region inset.

(J and K) Ce and Pr elemental maps, respectively, of the MVB (1.8 nm/pixel; five-window method on CCD detector (bin by four pixels) using a sum of six drift-corrected 40 s exposures, smoothed with Gaussian blur radius 1).

(L) Two-color merge of the Ce (green) and Pr (red) elemental maps), overlaid on a TEM image showing vesicular but no cytoplasmic RAB5A.

were treated with BILN-2061 and analyzed similarly (Figures 5G–5I) showed only a minimal signal for Ce by EELS in synapses (Figure 5J) despite comparable postsynaptic density staining in conventional EM.

DISCUSSION

In summary, we have developed a method that permits concurrent and selective visualization by EELS and EFTEM of two cellular components that can be labeled by photosensitizing fluorescent tracers or by peroxidases that can oxidize Ln-DAB2. Many fluorescent dyes are known to generate sufficient singlet oxygen via triplet sensitization of molecular oxygen so the method should be of wide scope. The use of genetically encoded singlet oxygen generators, such as miniSOG when fused to proteins of interest, also permits the selective visualization by fluorescence and correlated EFTEM of their cellular localization in samples ranging from tissue culture cells to complex tissues such as the mammalian brain. Ln-DAB2 is efficiently precipitated by HRP for immunoperoxidase labeling but with some

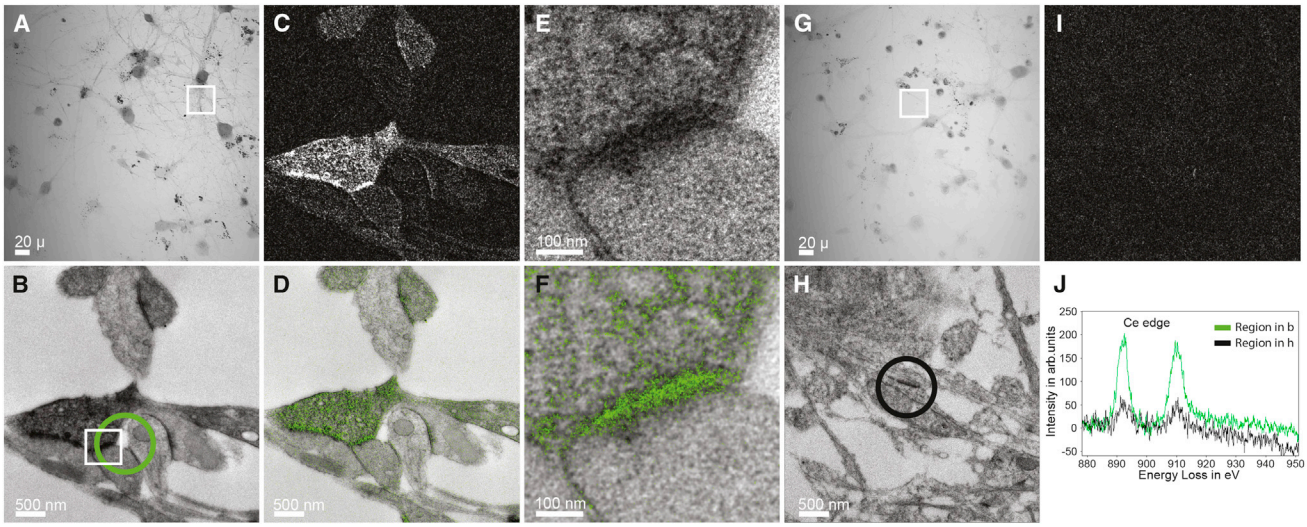

Figure 5. Chemical Long-Term Potentiation Results in PKMζ Localization to the Postsynaptic Membrane

(A) Transmitted light image of photooxidized cultured neurons expressing TS:YSOG3-PKMζ, stimulated with forskolin and rolipram, treated with BILN-2061 for 24 hr, and photooxidized with Ce-DAB2.

(B) TEM image (0.9 nm/pixel) of a neuron (white box in A) showing enhanced postsynaptic electron density.

(C) Ce elemental map acquired on CCD (4.4 nm/pixel; three-window method using a sum of seven drift-corrected 40 s exposures per window, smoothed with a Gaussian blur 1) showing that Ce localization corresponds to photooxidation and confirming that PKMζ strongly localizes to the postsynaptic membrane after stimulation.

(D) Overlay of the Ce map (green) on the TEM image.

(E) TEM image at a higher magnification of the region shown in (B) (white box).

(F) Overlay of the Ce map at higher magnification (0.2 nm/pixel; three-window method using a sum of 25 drift-corrected 50 s exposures per window, smoothed with Gaussian blur 3) on the TEM image.

(G) Transmitted light image of unstimulated neurons expressing TS:YSOG3-PKMζ treated with BILN-2061 for 24 hr and photooxidized with Ce-DAB2.

(H) TEM image of the neuron shown in (G) (white box).

(I) Ce elemental map acquired on DE-12 detector (4.4 nm/pixel; three-window method using a sum of seven drift-corrected 40 s exposures per window, smoothed with a Gaussian blur 1) of the region in (H) scaled similarly to (C) indicating minimal Ce deposition, and that basally produced TS:YSOG3-PKMζ is not postsynaptically localized in the image.

(J) EELS quantification of the relative Ce signal spectra of the circular regions shown in (B) (green circle) and (H) (black circle), normalized to the same background counts.

limitations. Unexpectedly, we found that HRP or its genetically encoded versions and the more recently developed APEX (Lam et al., 2015; Martell et al., 2012), a mutated ascorbate peroxidase, act as photosensitizers and precipitate Ln-DAB2 (or DAB) when illuminated between 400 and 650 nm (data not shown). This property limits their use with multicolor EM unless they are introduced after the first round of Ln-DAB2 photooxidation, as described above (Figures 2 and 3). Both peroxidases contain a heme prosthetic group that has not been reported to photosensitize molecular oxygen but, if insufficient heme is available in the cell, protoporphyrin IX (Durner and Klessig, 1995) is known to bind both HRP and APEX (Jullian et al., 1989; Lam et al., 2015; Martell et al., 2012). We speculate that trace-bound amounts of this efficient photosensitizer (Fernandez et al., 1997) are responsible for the photooxidation of Ln-DAB2 by these enzymes over the range of illuminating wavelengths that match that of protoporphyrin IX absorbance. APEX2 was engineered to improve heme binding but still deposited DAB upon illumination. Chemical inactivation (Durner and Klessig, 1995) of APEX2 to permit a second Ln-DAB2 to be photooxidized by another photosensitizer was ineffective. Further mutation of APEX or methods for increasing cellular heme availability during APEX expression will probably be required for their use in multicolor EM. Despite these limitations, multicolor EM has demonstrated the feasibility of selective deposition of metals by DAB oxidizers that are organelle stains, genetically targetable or encodable, or immunoreactive. EFTEM, although predominately used today for chemical analysis of materials, has been applied to biological samples using the generally weak signals from endogenous elements (Aronova and Leapman, 2012), but is sufficiently sensitive to detect and distinguish many of the 14 stable lanthanides when precipitated as Ln-DAB2. The sensitivity of the method is probably not limited by Ln-DAB oxidation as it photooxidizes at a comparable rate to DAB which can yield close to single-molecule detectability after extended illumination, staining with osmium, and conventional TEM (our unpublished results). There is negligible Ln background signal in EELS spectra of non-photooxidized cells, so similar sensitivity might be expected, but EELS is an inherently insensitive technique. The major current limitation is probably the noise introduced by sample drift during the long energy-filtered exposures required for the images.

Improvements are underway to boost the sensitivity of multicolor EM by increasing the amount of lanthanide that

is deposited during the oxidation of Ln-DAB chelates. Further development should lead to a greater understanding of the relationship between structure and metal deposition and will improve signal-to-noise, decrease acquisition time and sample damage, and potentially permit greater resolution through tomography. The use of DAB to precipitate metals limits the scope of photooxidation because the polymer itself acts as a photosensitizer of further DAB oxidation up to about 600 nm, and limits the number of different Ln-DABS that can be successively deposited by spectrally distinct photosensitizers. Acylation of unreacted amino groups in the Ln-DAB precipitate diminished its undesired reaction with a subsequent Ln-DAB Efforts are underway to completely chemically block it and the photosensitizing effects of precipitated Ln-DAB, and thereby eliminate the present requirement for deconvolution that can be problematic when the elemental signals are all co-localized.

SIGNIFICANCE

Major improvements in multicolor and super-resolution fluorescence microscopy over the last two decades have dramatically improved our understanding of cellular microarchitecture and function. Comparable progress in electron microscopy has been achieved in throughput and automation, but methods for marking multiple molecules of interest have been more limited. This work describes a new methodology for such selective detection or painting by sequential localized oxidation and precipitation of diaminobenzidine conjugates of Ln chelates by genetically encoded photosensitizers, small-molecule probes, or peroxidases. Electron energy-loss spectroscopy of these orthogonally deposited lanthanide metals and their imaging by energy-filtered transmission electron microscopy yields elemental maps that can be displayed on conventional electron micrographs as color overlays.

EXPERIMENTAL PROCEDURES

Reagents and solvents were from Sigma-Aldrich and cell culture reagents and probes were obtained from Life Technologies except where noted. All animal procedures were approved by the Institutional Animal Care and Use Committee of the University of California, San Diego.

Synthesis of Ln-DAB2

Diethylene-triamine-N,N′,N″-triacetic acid bis(diaminobenzidine)amide, DTPA-DAB_2: DTPA bis-anhydride (3.33 g, 9.33 mmol) suspended in dry DMF (33 mL) with triethylamine (1.30 mL, 9.33 mmol) under N_2 was gently heated and bath sonicated until dissolved. After cooling to room temperature, the solution was added dropwise over 30 min with stirring under N_2, to DAB (10 g, 46.65 mmol) and triethylamine (18.66 mmol, 2.60 mL) dissolved in dry DMF (33 mL). After stirring overnight at room temperature, the reaction mix was evaporated, dissolved in water (100 mL), and adjusted to pH 8 with 1 N NaOH until the pH stabilized (about 15 min). The mixture was stirred under N_2 for 1 hr, and then unreacted DAB was removed by filtration followed by extraction with EtOAc (3 × 100 mL). The aqueous layer was partially evaporated to remove EtOAc and then acidified to pH 5.4 with a concentration of HCl to give the product as a gray precipitate, which was collected by filtration and washed with water. Drying over P_2O_5 in vacuo overnight gave 2.75 g (38%) of a gray solid that was used without further purification. LC-MS indicated 70%–80% purity with unreacted DAB as the remainder (Figure S2).

Ln-DAB2 Solutions

Ln-DAB2 solutions in cacodylate buffer were prepared immediately before use at room temperature. To make 10 mL of a 2 mM Ln, Ce, or Pr-DAB2 solution, 15.6 mg (20 μmol) of DTPA-DAB_2 was suspended in DMF (0.25 mL) and sonicated/vortexed to disperse. Water (8.33 mL) was added to give a cloudy solution that cleared on addition of $LnCl_3$ aqueous solution (0.1 M of $LaCl_3 \cdot 6H_2O$, $CeCl_3 \cdot 6H_2O$, or $PrCl_3 \cdot xH_2O$; the latter stock solution was dissolved in 0.1 M HCl) with 120 μL of La or Ce solutions or 140 μL of Pr solution, followed by vortexing and bath sonication to give clear light-brown solutions. Aqueous NaOH solution (1 M) was added sequentially in six equal portions (6 × 10 μL) with vortexing after each addition. A precipitate was initially formed during the early steps of this neutralization but a mostly clear solution was present by the end. Cacodylate buffer (1.67 mL of 0.3 M sodium cacodylate [pH 7.4]) was added, mixed, and centrifuged (3000 × *g*, 10 min) to remove any precipitate. Solutions were syringe-filtered (0.22 μm, Millipore) immediately prior to addition to cells. Metal ion concentrations were measured by inductively coupled plasma mass spectroscopy (Agilent 7700).

Synthesis of Arg_{10}-IRDye 700DX

Arg_{10}-IRDye 700DX was prepared by reaction of H_2N-GGRRRRRRRRRR-$CONH_2$ (where G and R are L-glycine and L-arginine, respectively; synthesized by standard Fmoc chemistry with a Protein Technologies Prelude peptide synthesizer), with IRDye 700DX NHS ester (LI-COR Biosciences) in DMSO and N-methylmorpholine as base. The conjugate was purified by reverse-phase HPLC and characterized by LC-MS. Found, 575.0 ($M + 6H^+$), 689.6 ($M + 5H^+$), 861.9 ($M + 4H^+$), 1,148.8 ($M + 3H^+$). Deconvolved to 3,343.6, calculated 3,443.5.

Eosin-Sensitized Photooxidation

A solution of DAB or Ln-DAB2 (0.4 mM, diluted from freshly prepared 100 mM stock solutions in DMF) and eosin (20 μM) in 100 mM 3-(N-morpholino)propanesulfonic acid sodium salt (pH 7.2), or 0.1 M sodium cacodylate (pH 7.4) in a 3-mL cuvette was irradiated at 480 nm (30 nm band pass) using a solar simulator (Spectra-Physics 92191-1000 solar simulator with 1,600 W mercury arc lamp and two Spectra-Physics SP66239-3767 dichroic mirrors to remove infrared and UV wavelengths). The remaining light was filtered through 10-cm-square band-pass filters (Chroma Technology) with a deflector mirror set at 45° while bubbling with air. At set time points, the absorbance of the reaction was measured at 650 nm until the increase was complete.

Cell Culturing, Labeling, and Transfection

MDCK and HEK293 cells were cultured on poly-D-lysine-coated 35-mm glass-bottom dishes (MatTEK) in DMEM supplemented with 10% fetal bovine serum. MDCK cells were labeled with 5 μM NBD C6-ceramide in medium containing 10% fetal calf serum for 30 min, washed, and incubated for 30 min in new culture medium, all at 37°C with 5% carbon dioxide, then washed (5 times) with Hank's balanced salt solution (HBSS) at 37°C. Cells were then incubated with mouse monoclonal EPCAM antibody (KS1/4) (Santa Cruz Biotechnology) at 1:1,000 dilution for 12 min at 37°C in HBSS, washed with HBSS, incubated for 60 min in secondary antibody-biotinylated goat anti-mouse immunoglobulin G (Jackson Laboratory, 115-065-003) at 1:250 dilution at 37°C in HBSS and then washed. HEK293 cells were transfected with a miniSOG-RAB5A plasmid at 60%–80% confluence using Lipofectamine 2000, which was removed after 8 hr. Cells were treated 48 hr after transfection with 2 μM Arg_{10}-IRDye 700DX (prepared in distilled water) and added to the culture medium for 2 hr at 37°C, after which time the medium was removed and cells were rinsed once in HBSS. Primary mouse cortical neurons were cultured, transfected with TS:YSOG3-PKMζ, and chemically stimulated with 50 μM forskolin and 0.1 μM rolipram for 10 min, then incubated with 1 μM BILN-2061 as described previously (Palida et al., 2015).

General Procedure for Photooxidation and HRP Reaction of Ln-DAB2

Labeled cells were fixed and blocked (Shu et al., 2011). Samples were then transferred either to a Bio-Rad MRC1024 with a Zeiss Axiovert 35M microscope or a Leica SPE microscope. MDCK cells stained with NBD C6-ceramide and transfected HEK293 cells exhibiting peptide uptake were identified either

by NBD C6-ceramide, miniSOG, or IRDye 700DX fluorescence, respectively, and imaged by confocal microscopy.

Freshly prepared and filtered La-DAB2 (2 mM) or Ce-DAB2 (2 mM) for the first photooxidation reaction was added to the dish of cells for 5 min while a stream of pure oxygen was gently blown continuously over the solution. Cells were irradiated to excite NBD C6-ceramide depositing La-DAB2 or miniSOG depositing Ce-DAB2 reaction product both using 450–490 nm excitation (Ex) and 515 nm emission (Em) long-pass (LP) filters with a 580 nm dichroic mirror. Reaction product formation was monitored by transmitted light microscopy and illumination was stopped as soon as a light-brown reaction product appeared. Acetic anhydride (MDCK cells) was added (20 × 20 mM freshly prepared) for 1 min each to block precipitated La-DAB2. Alternatively, MDCK cells were rinsed 3 × 5 min with fresh 100 mM acetylimidazole in 0.15 M NaCl to prevent further polymerization of either La-DAB2 or Ce-DAB2, then treated with freshly prepared Ce-DAB2 (2 mM) for HRP enzymatic reaction, or irradiated to excite IRDye 700DX (Ex 675/67 nm, Em, 736 LP) depositing Pr-DAB2 reaction product. Cells were rinsed 5 × 2 min, postfixed, dehydrated, infiltrated, and embedded as described previously (Shu et al., 2011).

Hippocampal Astrocyte Filling with Lucifer Yellow and Neurobiotin

Intracellular Astrocyte Filling with Fluorescent Dyes in Fixed Tissue

A mouse (2-month-old BALB/c male) was perfused with Ringers, followed by 4% paraformaldehyde, 0.2% glutaraldehyde in 0.1 M PBS (Bushong et al., 2002). Coronal slices (100 μm thick) were cut through the hippocampus using a vibratome. In the CA1 stratum radiatum, one astrocyte was iontophoretically injected with 5% lucifer yellow-CH in water and an adjacent astrocyte was injected with 2.5% Alexa Fluor 568/2% neurobiotin (Vector, SP-1120) in 200 mM KCl (Bushong et al., 2002). The tissue slices were then postfixed with 4% paraformaldehyde/0.2% glutaraldehyde in 0.1 M PBS. Confocal volumes were taken of the filled astrocytes with a Leica SPE inverted confocal microscope, and the slices were further fixed with 2.0% glutaraldehyde in 0.15 M sodium cacodylate buffer for 10 min on ice, followed by washing several times with 0.15 M sodium cacodylate buffer (pH 7.4).

Photooxidation of Lucifer Yellow Filled Astrocytes

Tissues were treated for 15 min in blocking buffer (50 mM glycine, 5 mM KCN, and 5 mM aminotriazole) to reduce nonspecific background reaction of DAB derivatives, filtered Ce-DAB2 solution was added to a tissue slice at room temperature and incubated for 10 min before photooxidation. A stream of pure oxygen was gently blown continuously over the solution. The lucifer yellow was then excited using a standard fluorescein isothiocyanate filter set (Ex 470/40, DM510, Em BA520) with intense light from a 150 W xenon lamp. Illumination was stopped as soon as a light-brown reaction product appeared within the filled astrocyte (8–10 min), as monitored by transmitted light.

Blocking of First Ln-DAB2 Product

Following photooxidation, each tissue slice was washed several times with cold 0.15 M sodium cacodylate buffer (pH 7.4) and then blocked with freshly prepared 100 mM acetylimidazole in 0.15 M sodium chloride (3 × 5 min).

HRP Labeling and Enzymatic Reaction of Photooxidized Cells

The tissues were incubated with cryoprotectant, then freeze-thawed to permeabilize the tissues (Knott et al., 2009). The tissues were washed several times with 0.15 M sodium cacodylate buffer (pH 7.4), incubated with 1% BSA in the cacodylate buffer for 30 min followed by overnight incubation with a Vectorstain Elite ABC staining kit (Vector, PK6100). After rinsing several times for 1 hr with cold 0.1 M cacodylate buffer (pH 7.4), 20 mL of Pr-DAB2 solution and 5 μL of 30% H_2O_2 were added to each tissue. After the neurobiotin-filled astrocyte turned brown, the tissue was washed several times with 0.15 M sodium cacodylate buffer (pH 7.4).

Tissue Processing for TEM

Tissues were fixed with 2% glutaraldehyde in cacodylate buffer for 20 min, washed several times with cacodylate buffer, postfixed with 0.5% of OsO_4 in cacodylate buffer for 30 min, dehydrated in an ethanol series of 0%, 20%, 50%, 70%, 90%, and 100% on ice for 5 min each, 100% ethanol twice for 5 min each at room temperature, 1:1 100% dry ethanol:dry acetone for 5 min, 100% dry acetone for 5 min, 50:50 dry acetone:Durcupan ACM for 30 min, four changes of Durcupan for 1 hr each, and embedded in a 60°C oven for 48 hr.

Section Preparation from Cells and Tissue

Sections (100 nm thick) were cut by an Ultra 45° Diatome diamond knife using a Leica Ultracut UCT ultramicrotome, and sections were picked up on a 50-mesh copper grid (Ted Pella, G50). Sections were carbon coated on both sides by a Cressington 208 carbon coater to prevent charging of the plastic which can cause drift and thermal damage.

Electron Microscopy

EFTEM was performed with a JEOL JEM-3200EF transmission electron microscope operating at either 200 or 300 KV, equipped with an in-column Omega filter and a LaB6 electron source. The samples were pre-irradiated at a low magnification of 100× for about 30 min to stabilize the sample and minimize contamination (Egerton et al., 2004). The elemental maps were obtained at the $M_{4,5}$ core-loss edge, the onset of which occurs at 832, 883, and 931 for lanthanum (La), cerium (Ce), and praseodymium (Pr), respectively (Ahn and Krivanek, 1983). The EFTEM images of the pre- and post-edges were obtained using a slit of 30 eV width. The electron energy-loss spectrum was acquired using the Ultrascan 4000 CCD detector from Gatan. The conventional images and elemental maps were acquired using both the Ultrascan 4000 detector and the direct detection device DE-12 from Direct Electron LP. See Supplemental Experimental Procedures for details.

Two-Color Elemental Map Merge and Overlay on TEM

Elemental maps and TEM were pre-aligned in Photoshop (Adobe) and merged pixel-by-pixel using the following custom algorithm running in C++.

$$(\text{Display Pixel})_{R,G,B} = (1 - T)\cdot(\text{Pixel}_{TEM})_{R,G,B} + T\cdot(\text{Pixel}_{OVR})_{R,G,B},$$

where Pixel_{TEM} is the 24-bit red-green-blue (RGB) coordinate for the gray scale TEM image, and Pixel_{OVR} is the 24-bit RGB coordinate for the overlay hue at maximum saturation and brightness. T is a transparency factor, the value of which determines what percentage of the overlay color coordinate contributes to the final display pixel. The color coordinate for Pixel_{OVR} is calculated in the HSL (hue, saturation, and lightness) color space. In the following example, the hue (H) for Pixel_{OVR} is determined using two EELS channels:

$$S_1 = I_1/(I_1 + I_2),$$

$$S_2 = I_2/(I_1 + I_2),$$

$$H = (S_1\cdot H_1) + (S_2\cdot H_2),$$

where S is a scale factor and I is the intensity of the signal for each respective channel, and H_1 and H_2 are the arbitrary hues selected for each channels (e.g., red and green).

The lightness (I) for Pixel_{OVR} is calculated as follows:

$$I = (S_1\cdot I_1) + (S_2\cdot I_2).$$

Finally, the RGB coordinate for Pixel_{OVR} is determined using an HSL to RGB color space conversion algorithm where S is set to maximum. The transparency factor is calculated as follows:

$$T = I/255,$$

The raw EELS data need to be scaled between 0 and 255 (8-bits) and should be done prior to implementing the algorithm.

SUPPLEMENTAL INFORMATION

Supplemental Information includes Supplemental Experimental Procedures and five figures and can be found with this article online at http://dx.doi.org/10.1016/j.chembiol.2016.10.006.

AUTHOR CONTRIBUTIONS

S.A., R.T., and M.E. conceived and designed the experiments, S.A., M.M., R.R., S.P., E.B., B.G., M.B., and P.S. performed all experiments and analyzed data, and S.A., M.M., R.R., and R.T. wrote the manuscript.

ACKNOWLEDGMENTS

We thank David Mastronarde (University of Colorado Boulder) and Liang Jin (Direct Electron) for help with scripting in Serial EM and DE-12 direct detection device, respectively, and James Bouwer, Thomas Deerinck, and Junru Hu for advice and technical assistance. This work was supported by UCSD Graduate Training Programs in Cellular and Molecular Pharmacology (T32 GM007752) (S.P.) and in Neuroplasticity of Aging (T32 AG000216) (S.P.), NIH GM103412 (M.E.), the W.M. Keck Foundation (M.E.), and NIH GM086197 (R.T.).

Received: June 13, 2016
Revised: August 16, 2016
Accepted: October 12, 2016
Published: November 3, 2016

REFERENCES

Ahn, C.C., and Krivanek, O.L. (1983). EELS Atlas (Gatan).

Aronova, M.A., and Leapman, R.D. (2012). Development of electron energy loss spectroscopy in the biological sciences. MRS Bull. *37*, 53–62.

Betzig, E., Patterson, G.H., Sougrat, R., Lindwasser, O.W., Olenych, S., Bonifacino, J.S., Davidson, M.W., Lippincott-Schwartz, J., and Hess, H.F. (2006). Imaging intracellular fluorescent proteins at nanometer resolution. Science *313*, 1642–1645.

Brock, R. (2014). The uptake of arginine-rich cell-penetrating peptides: putting the puzzle together. Bioconjug. Chem. *25*, 863–868.

Bushong, E.A., Martone, M.E., Jones, Y.Z., and Ellisman, M.H. (2002). Protoplasmic astrocytes in CA1 stratum radiatum occupy separate anatomical domains. J. Neurosci. *22*, 183–192.

Bushong, E.A., Martone, M.E., and Ellisman, M.H. (2004). Maturation of astrocyte morphology and the establishment of astrocyte domains during postnatal hippocampal development. Int. J. Dev. Neurosci. *22*, 73–86.

Butko, M.T., Yang, J., Geng, Y., Kim, H.J., Jeon, N.L., Shu, X., Mackey, M.R., Ellisman, M.H., Tsien, R.Y., and Lin, M.Z. (2012). Fluorescent and photooxidizing TimeSTAMP tags track protein fates in light and electron microscopy. Nat. Neurosci. *15*, 1742–1751.

Copolovici, D.M., Langel, K., Eriste, E., and Langel, Ü. (2014). Cell-penetrating peptides: design, synthesis, and applications. ACS Nano *8*, 1972–1994.

Deerinck, T.J., Martone, M.E., Levram, V., Green, D.P.L., Tsien, R.Y., Spector, D.L., Huang, S., and Ellisman, M.H. (1994). Fluorescence photooxidation with Eosin - a method of high-resolution immunolocalization and in-situ hybridization detection for light and electron-microscopy. J. Cell Biol. *126*, 901–910.

Durner, J., and Klessig, D.F. (1995). Inhibition of ascorbate peroxidase by salicylic acid and 2,6-dichloroisonicotinic acid, two inducers of plant defense responses. Proc. Natl. Acad. Sci. USA *92*, 11312–11316.

Egerton, R.F. (1996). Electron Energy-loss Spectroscopy (Plenum Press).

Egerton, R.F., Li, P., and Malac, M. (2004). Radiation damage in the TEM and SEM. Micron *35*, 399–409.

Fernandez, J.M., Bilgin, M.D., and Grossweiner, L.I. (1997). Singlet oxygen generation by photodynamic agents. J. Photochem. Photobiol. B Biol. *37*, 131–140.

Gaietta, G., Deerinck, T.J., Adams, S.R., Bouwer, J., Tour, O., Laird, D.W., Sosinsky, G.E., Tsien, R.Y., and Ellisman, M.H. (2002). Multicolor and electron microscopic imaging of connexin trafficking. Science *296*, 503–507.

Geze, C., Mouro, C., Hindre, F., LePlouzennec, M., Moinet, C., Rolland, R., Alderighi, L., Vacca, A., and Simonneaux, G. (1996). Synthesis, characterization and relaxivity of functionalized aromatic amide DTPA-lanthanide complexes. Bull. Soc. Chim. Fr. *133*, 267–272.

Halassa, M.M., Fellin, T., Takano, H., Dong, J.H., and Haydon, P.G. (2007). Synaptic islands defined by the territory of a single astrocyte. J. Neurosci. *27*, 6473–6477.

Haydon, P.G. (2001). GLIA: listening and talking to the synapse. Nat. Rev. Neurosci. *2*, 185–193.

Haydon, P.G., and Carmignoto, G. (2006). Astrocyte control of synaptic transmission and neurovascular coupling. Physiol. Rev. *86*, 1009–1031.

Hell, S.W. (2007). Far-field optical nanoscopy. Science *316*, 1153–1158.

Hernández, A.I., Oxberry, W.C., Crary, J.F., Mirra, S.S., and Sacktor, T.C. (2014). Cellular and subcellular localization of PKMζ. Philos. Trans. R. Soc. Lond. B Biol. Sci. *369*, 20130140.

Huang, B., Bates, M., and Zhuang, X. (2009). Super-resolution fluorescence microscopy. Annu. Rev. Biochem. *78*, 993–1016.

Jullian, C., Brunet, J.E., Thomas, V., and Jameson, D.M. (1989). Time-resolved fluorescence studies on protoporphyrin IX-apohorseradish peroxidase. Biochim. Biophys. Acta *997*, 206–210.

Kaplan, I.M., Wadia, J.S., and Dowdy, S.F. (2005). Cationic TAT peptide transduction domain enters cells by macropinocytosis. J. Control. Release *102*, 247–253.

Knott, G.W., Holtmaat, A., Trachtenberg, J.T., Svoboda, K., and Welker, E. (2009). A protocol for preparing GFP-labeled neurons previously imaged in vivo and in slice preparations for light and electron microscopic analysis. Nat. Protoc. *4*, 1145–1156.

Kuipers, J., van Ham, T.J., Kalicharan, R.D., Veenstra-Algra, A., Sjollema, K.A., Dijk, F., Schnell, U., and Giepmans, B.N. (2015). FLIPPER, a combinatorial probe for correlated live imaging and electron microscopy, allows identification and quantitative analysis of various cells and organelles. Cell Tissue Res. *360*, 61–70.

Lam, S.S., Martell, J.D., Kamer, K.J., Deerinck, T.J., Ellisman, M.H., Mootha, V.K., and Ting, A.Y. (2015). Directed evolution of APEX2 for electron microscopy and proximity labeling. Nat. Methods *12*, 51–54.

Maranto, A.R. (1982). Neuronal mapping: a photooxidation reaction makes Lucifer yellow useful for electron microscopy. Science *217*, 953–955.

Martell, J.D., Deerinck, T.J., Sancak, Y., Poulos, T.L., Mootha, V.K., Sosinsky, G.E., Ellisman, M.H., and Ting, A.Y. (2012). Engineered ascorbate peroxidase as a genetically encoded reporter for electron microscopy. Nat. Biotechnol. *30*, 1143–1148.

Mitsunaga, M., Ogawa, M., Kosaka, N., Rosenblum, L.T., Choyke, P.L., and Kobayashi, H. (2011). Cancer cell-selective in vivo near infrared photoimmunotherapy targeting specific membrane molecules. Nat. Med. *17*, 1685–1691.

Natera, J., Massad, W., Amat-Guerri, F., and Garcia, N. (2011). Elementary processes in the eosin-sensitized photooxidation of 3,3 '-diaminobenzidine for correlative fluorescence and electron microscopy. J. Photochem. Photobiol. Chem. *220*, 25–30.

Oakenfull, D., and Jencks, W. (1971). Reactions of acetylimidazole and acetylimidazolium ion with nucleophilic reagents - structure-reactivity relationships. J. Am. Chem. Soc. *93*, 178–188.

Pagano, R.E., Sepanski, M.A., and Martin, O.C. (1989). Molecular trapping of a fluorescent ceramide analogue at the Golgi apparatus of fixed cells: interaction with endogenous lipids provides a trans-Golgi marker for both light and electron microscopy. J. Cell Biol. *109*, 2067–2079.

Pagano, R.E., Martin, O.C., Kang, H.C., and Haugland, R.P. (1991). A novel fluorescent ceramide analogue for studying membrane traffic in animal cells: accumulation at the Golgi apparatus results in altered spectral properties of the sphingolipid precursor. J. Cell Biol. *113*, 1267–1279.

Palida, S.F., Butko, M.T., Ngo, J.T., Mackey, M.R., Gross, L.A., Ellisman, M.H., and Tsien, R.Y. (2015). PKMζ, but not PKCλ, is rapidly synthesized and degraded at the neuronal synapse. J. Neurosci. *35*, 7736–7749.

Peng, X., Draney, D., Volcheck, W., Bashford, G., Lamb, D., Grone, D., Zhang, Y., Johnson, C., Achilefu, S., Bornhop, D., et al. (2006). Phthalocyanine dye as an extremely photostable and highly fluorescent near-infrared labeling reagent - art. no. 60970E. Opt. Mol. Probes Biomed. Appl. *6097*, E970.

Richard, J.P., Melikov, K., Vives, E., Ramos, C., Verbeure, B., Gait, M.J., Chernomordik, L.V., and Lebleu, B. (2003). Cell-penetrating peptides. A reevaluation of the mechanism of cellular uptake. J. Biol. Chem. *278*, 585–590.

Rink, J., Ghigo, E., Kalaidzidis, Y., and Zerial, M. (2005). Rab conversion as a mechanism of progression from early to late endosomes. Cell *122*, 735–749.

Schnell, U., Dijk, F., Sjollema, K.A., and Giepmans, B.N. (2012). Immunolabeling artifacts and the need for live-cell imaging. Nat. Methods *9*, 152–158.

Schnell, U., Cirulli, V., and Giepmans, B.N. (2013). EpCAM: structure and function in health and disease. Biochim. Biophys. Acta *1828*, 1989–2001.

Shao, C.Y., Sondhi, R., van de Nes, P.S., and Sacktor, T.C. (2012). PKMζ is necessary and sufficient for synaptic clustering of PSD-95. Hippocampus *22*, 1501–1507.

Shu, X.K., Lev-Ram, V., Deerinck, T.J., Qi, Y.C., Ramko, E.B., Davidson, M.W., Jin, Y.S., Ellisman, M.H., and Tsien, R.Y. (2011). A genetically encoded tag for correlated light and electron microscopy of intact cells, tissues, and organisms. PLoS Biol. *9*, 10.

Takizawa, P.A., Yucel, J.K., Veit, B., Faulkner, D.J., Deerinck, T., Soto, G., Ellisman, M., and Malhotra, V. (1993). Complete vesiculation of Golgi membranes and inhibition of protein transport by a novel sea sponge metabolite, ilimaquinone. Cell *73*, 1079–1090.

Cell Chemical Biology, Volume *23*

Supplemental Information

Multicolor Electron Microscopy for Simultaneous Visualization of Multiple Molecular Species

Stephen R. Adams, Mason R. Mackey, Ranjan Ramachandra, Sakina F. Palida Lemieux, Paul Steinbach, Eric A. Bushong, Margaret T. Butko, Ben N.G. Giepmans, Mark H. Ellisman, and Roger Y. Tsien

Supplemental Data

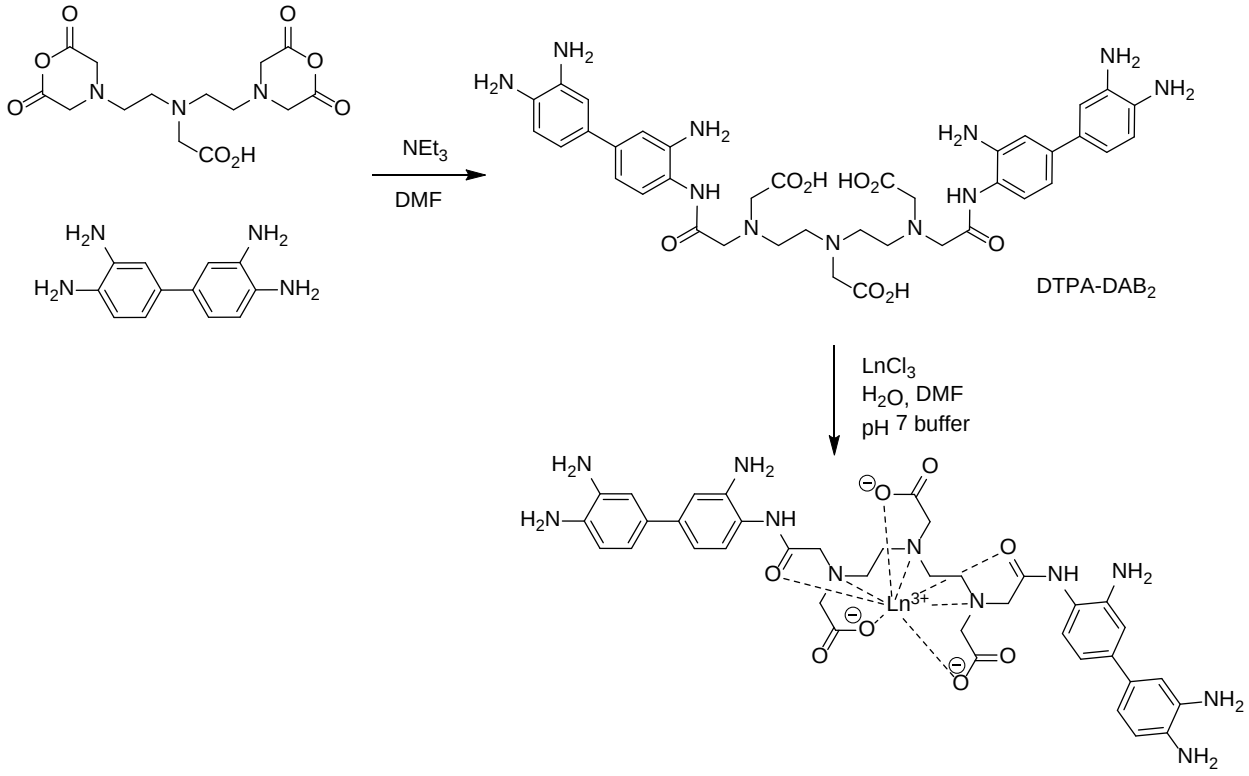

Figure S1 (related to Experimental Procedures): Synthesis of Ln-DAB from the reaction of DTPA anhydride and DAB to form DTPA-DAB_2 and subsequent chelation of Ln^{3+}. Only one of the many possible positional isomers of the product is drawn for clarity.

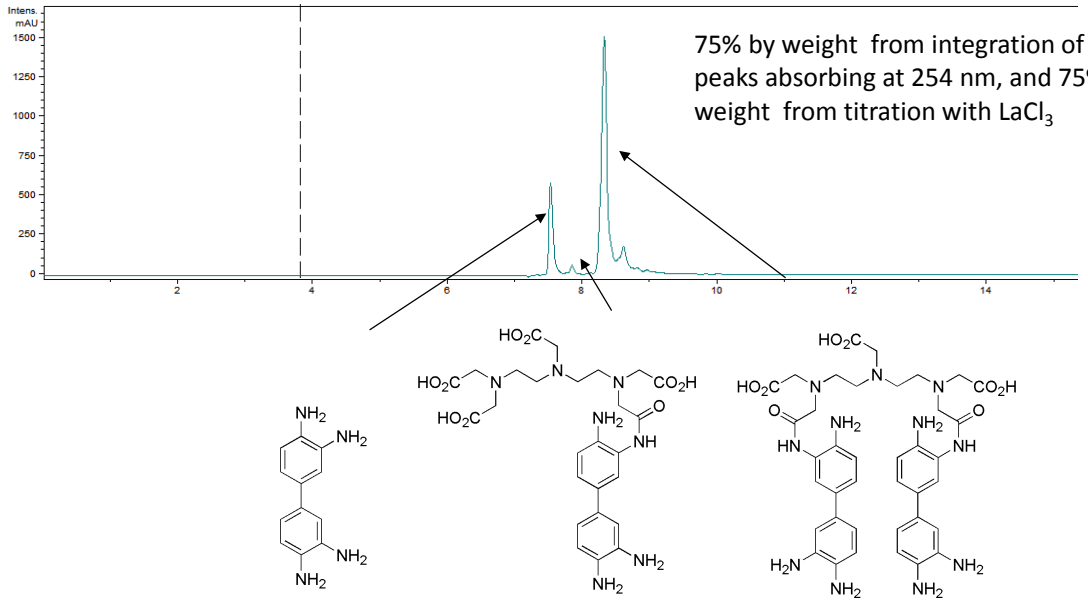

Figure S2 (related to Experimental Procedures): Reverse-phase HPLC analysis of dtpa-dab$_2$ with peak identification by electro-spray mass spectroscopy.

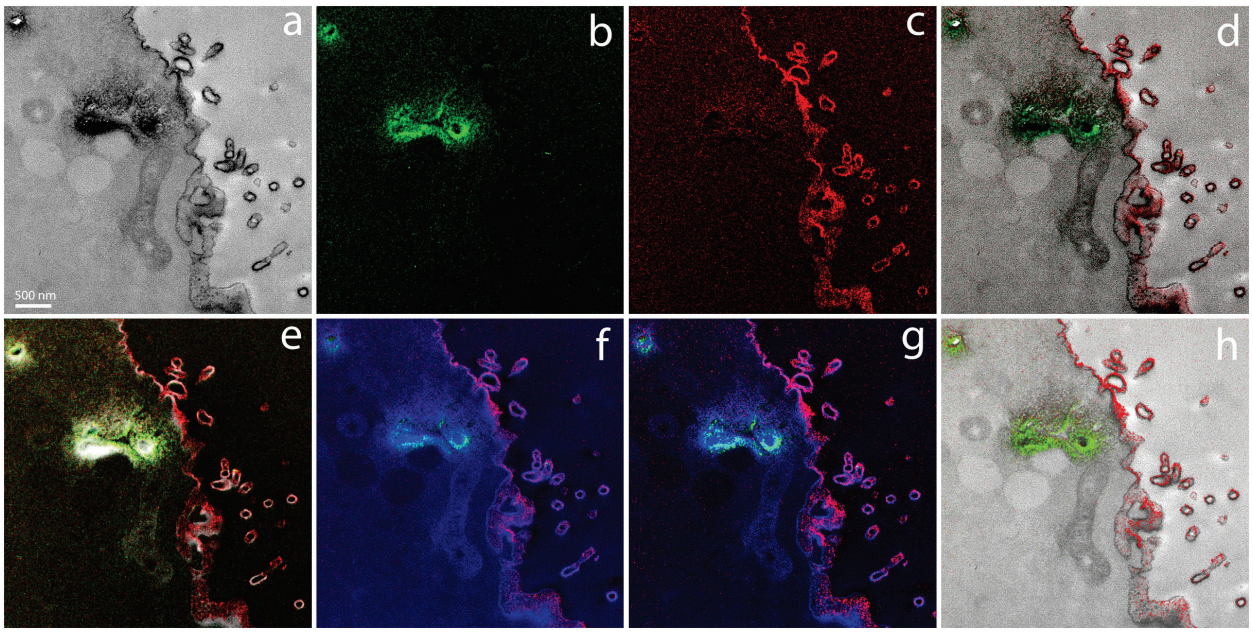

Figure S3 (related to Figure 2): a) Conventional TEM image (x 6000, 1.4 nm/pixel) of MDCK cell following photooxidation with La-DAB2 by NBD-ceramide labeled Golgi and subsequent oxidation of Ce-DAB2 on plasma membrane (PM) with HRP-labeled antibody to EpCAM. b) Corresponding green pseudocolored lanthanum elemental map c) Red pseudocolored cerium elemental map corrected for extraneous Ce precipitation at previously-deposited Ln-DAB2. d) Ln (green) and Ce (red) elemental map overlays on conventional grey-scale TEM e) Ln (green) and Ce (red) elemental map overlays on inverted conventional TEM. f) The merged green (La) and red (Ce) channels overlaid over the conventional TEM image as the blue channel. g) As f) but with exposure and tonal values of the blue channel altered to get the best visual effect. h) The merged green (La) and red (Ce) channels overlaid over the grayscale conventional TEM image using the custom software developed for this purpose (See text for more details).

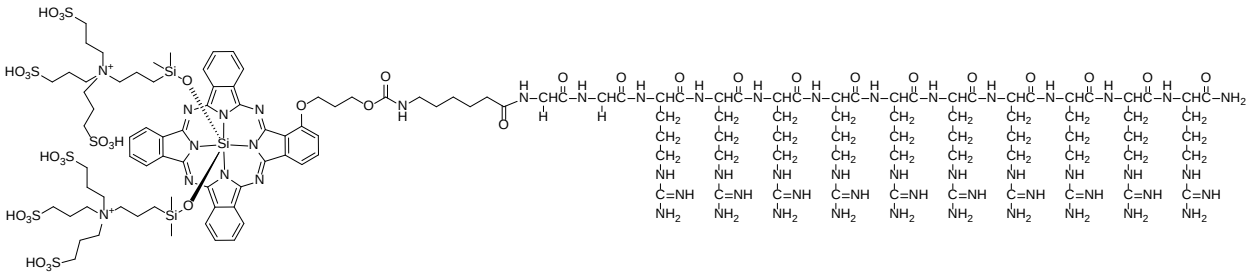

Chemical Formula: $C_{134}H_{226}N_{54}O_{36}S_6Si_3^{2+}$
Exact Mass: 3443.51
Molecular Weight: 3446.21

Figure S4 (related to Experimental Procedures and Figure 4): Chemical structure of Arg_{10}-IRDye700DX

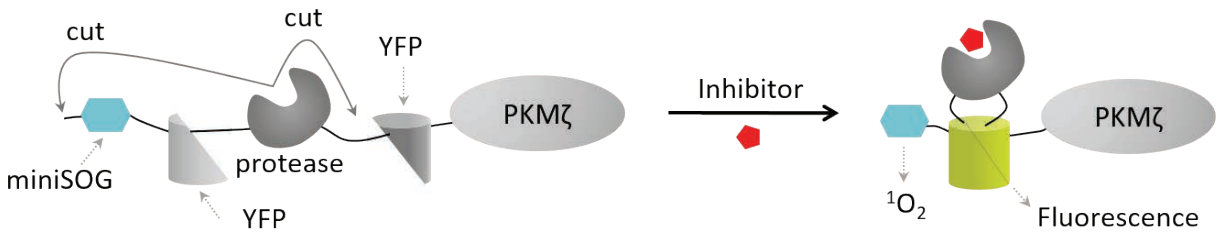

Figure S5 (related to Figure 5): Scheme of the generation of a fluorescent photosensitizer by Timestamp reporter fused to PKMζ following treatment with HCV protease inhibitor. In the absence of inhibitor, the protease embedded in the TS:YSOG3-PKMζ reporter cleaves at two sites; the split YFP does not complement and the miniSOG peptide is degraded. When an inhibitor to the protease is added, the split YFP reconstitutes and becomes fluorescent, marking new copies of protein visible by YFP fluorescence while also retaining miniSOG for EM.

Supplemental Experimental Procedures

Energy-filtered transmission electron microscopy (EFTEM) image acquisition

Traditionally, the core-loss elemental maps are obtained using the three-window method (Egerton, 1996), two pre-edge images for computation of the background and a post-edge image acquired on the core-loss signal. For the two-color labeling, the two lanthanide metals used are adjacent metals in the periodic table (either La and Ce or Ce and Pr), and there was a spectrum bleed-through of the metal with lower atomic number, showing up as a faded/faint signal in the elemental map of the higher atomic number lanthanide metal. This signal bleed-through was mainly due to the inaccurate background extrapolation in the three-window method. We devised a five-window method that uses four EFTEM images instead of two for interpolating the background. This estimate is a more precise statistical fit of background and therefore, minimizes any effects of signal bleed-through in the elemental maps. The five-window consists of two pre-edge and a post-edge image as before, but in addition has two EFTEM images obtained after the core-loss peak, which we will refer to as after-peak images. The elemental maps were computed using the EFTEM-TomoJ plug-in of ImageJ (Messaoudi, et al., 2013), the background fit was computed using the two pre-edge and the two after-peak image using the power law fit.

The electron energy-loss spectrum was acquired using the Ultrascan 4000 CCD detector from Gatan (Pleasanton, CA, USA). The conventional images and elemental maps were acquired using both the Ultrascan 4000 detector and the direct detection device (DDD) DE-12 from Direct Electron LP. (San Diego, CA). The DE-12 detector has a high modulation transfer function (MTF) and provides better spatial resolution (Jin et al., 2008), but is ~1/3 the size of Ultrascan 4000 detector and therefore, has a much smaller field of view. The EFTEM images obtained with the Ultrascan 4000 detector were binned by 4 x 4 pixels to improve the SNR, no binning was applied to images obtained with the DE-12 detector. Also, the EFTEM images obtained with the Ultrascan 4000 detector were dark current subtracted and flatfield corrected, the DE-12 EFTEM images were only dark current subtracted.

To get reasonable SNR in core-loss EFTEM images, exposures exceeding several minutes are generally required. As specimen and aperture drift during such long exposures often deteriorates the image quality, an efficient alternative is to obtain series of short exposure images, and use drift correction to subsequently align and merge these individual images to form a single image (Aoyama, et al., 2002; Heil and Kohl, 2010; Ramachandra, et al., 2014; Schaffer, et al., 2004; Terada, et al., 2001). The drift in the images was calculated using the Template Matching plug-in in ImageJ (Tseng, et al., 2011); however, for datasets with very low signal or absence of sharp features this method did not yield satisfactory results. For such datasets, gold nanoparticles dispersed on the samples were used as fiducial markers for alignment using MTrackJ plugin of ImageJ (Meijering, et al., 2012). For calculation of drift vectors, a Gaussian blur of radius 0.7 – 3 pixels were applied to calculate the drift vectors only, and final merged image was obtained from the drift corrected raw images without any Gaussian blur.

Initially, the entire series of the EFTEM images were collected at one energy window before proceeding to the next energy window, in a sequential manner. However, this had the disadvantage that if sample shrinkage or warping occurred during the acquisition of a particular energy window, then it subsequently caused the elemental map to have image artifacts in the form of appearance of shadow at certain regions. We devised an alternate methodology, by which we acquire a set of short exposure images successively through all the energy windows and then acquire the next set through all the energy windows and so on. This interlaced acquisition has the advantage over sequential acquisition, that any sample shrinkage/warping and high tension instabilities over time, affected the images through all the energy windows equally. This acquisition routine was automated by writing macro's in Digital Micrograph (Gatan, Inc) and Serial EM (Mastronarde, 2005) for the control of Ultrascan 4000 and DE-12 detectors respectively. All elemental maps are obtained through the interlaced acquisition routine unless otherwise mentioned explicitly.

The Ultrascan 4000 is a scintillator based CCD detector, and EFTEM images acquired from them are susceptible to point blemishes occurring as bright pixels, caused by spurious X-rays hitting the scintillator screen (Anderson, 2008). Most of the point blemishes are single binned pixels (i.e. 4 x 4 pixels), and occasionally can spread to 2 – 4 binned pixels. These are undesirable, as they tend to skew the histogram of the elemental maps. To mitigate the effect of these point blemishes, a simple image processing routine was developed in Digital Micrograph. A region with the highest signal in the pre-edge1 image was selected, the mean (μ) and standard deviation (σ) of signal in this region was measured. The counts on each pixel (i.e., pixel intensity) for all the raw EFTEM images of the dataset was checked to see if its value was greater than μ and if the gradient with its four diagonal pixels was greater than

7σ; if so it was marked as a bright pixel or point blemish and its intensity was changed to the average of its four diagonal pixels. The number of point blemish typically varied from 2 – 10 binned pixels/image and 40 – 150 binned pixels/image (1k x 1k) at 200 KV and 300KV respectively, depending on the sample and acquisition conditions. The effect of X rays on the EFTEM images acquired on the DE-12 detector is negligible and no correction was required for them (Ramachandra, et al., 2014).

EFTEM acquisition parameters:

For the core-loss EFTEM images of the MDCK cells (NBD ceramide/EpCAM) sample, a series of nine images with a 60 s exposure/image, was acquired by the Ultrascan 4000 detector at 200 KV and a magnification of 8kX (pixel size 4.4 nm) for each energy window. The pre-edge and after-peak images were obtained at energy shifts of 758, 804, 947 and 990 eV. The La and Ce post-edge images were obtained at 850 and 902 eV respectively. The EFTEM images were acquired at a beam dose rate of ~ 9.8 X 10^{-5} PA/nm^2 and the total beam dose for the acquisition was ~ 2.0 X 10^6 e^-/ nm^2.

For the core-loss EFTEM images (i.e. pre-edge, post-edge and after-peak images) of the astrocyte sample, a series of 19 images for each energy window with a 50 s exposure/image, was acquired by the DE-12 detector at 300 KV, and at a magnification of 12kX (pixel size 0.42 nm). The pre-edge and after-peak images were obtained at an energy shift of 815, 855, 995 and 1030 eV. The Ce and Pr post-edge images were obtained at 899 and 947 eV respectively. The EFTEM images were acquired at a beam dose rate of ~ 1.9 X 10^{-4} PA/nm^2 and the total beam dose for the acquisition was ~ 6.9 X 10^6 e^-/ nm^2.

For the core-loss EFTEM images of the regular endosome sample, a series of 12 images for each energy window with a 50 sec exposure/image, was acquired by the DE-12 detector at 300 KV, and at a magnification of 25kX (pixel size 0.2 nm). The pre-edge and after-peak images were obtained at energy shifts of 815, 860, 985 and 1030 eV. The Ce and Pr post-edge images were obtained at 899 and 947 eV respectively. The energy windows were not acquired through the interlaced acquisition procedure, but rather sequentially. Gold nanoparticles (15 nm) were dispersed on the section to facilitate drift alignment. The EFTEM images were acquired at a beam dose rate of ~ 1.9 X 10^{-3} PA/nm^2 and the total beam dose for the acquisition was ~ 4.4 X 10^7 e^-/ nm^2.

For the core-loss EFTEM images of the multivesicular bodies, a series of five images for each energy window with a 60 sec exposure/image, was acquired by the Ultrascan 4000 detector at 300 KV and at a magnification of 20kX (pixel size 1.8 nm). The pre-edge and after-peak images were obtained at energy shifts of 815, 850, 995 and 1030 eV. The Ce and Pr post-edge images were obtained at 899 and 947 eV respectively. The EFTEM images were acquired at a beam dose rate of ~ 5.4 X 10^{-4} PA/nm^2 and the total beam dose for the acquisition was ~ 6.0 X 10^6 e^-/ nm^2.

For the PKMζ localization in cultured neurons (stimulated cell), a series of seven images for each energy window each at 40 s exposure, was acquired by the Ultrascan 4000 detector at 300 KV, and at a magnification of 8kX (unbinned pixel size 4.4 nm). The pre-edge and after-peak images were obtained at energy shifts of 815, 855, 995 and 1040 eV. The Ce post-edge images were obtained 899 eV. A second set of higher resolution EFTEM maps was obtained on the same region and with the same energy windows, at a magnification of 25 kX (unbinned pixel size 0.2 nm) by the DE-12 detector at 200 KV. For this dataset, a series of 25 images for each energy window with a 50 s exposure/image was acquired. The EFTEM images on the Ultrascan 4000 were acquired at a beam dose rate of ~ 1.8 X 10^{-4} PA/nm^2 and the total beam dose for the acquisition was ~ 1.9 X 10^6 e^-/ nm^2. The EFTEM images on the DE-12 were acquired at a beam dose rate of ~ 1.4 X 10^{-3} PA/nm^2 and the total beam dose for the acquisition was ~ 6.4 X 10^7 e^-/ nm^2.

For the PKMζ localization in cultured neurons (unstimulated cell), a series of seven images for each energy window with a 40 s exposure/image was acquired by the Ultrascan 4000 detector at 300 KV, and at a magnification of 8kX (unbinned pixel size 4.4 nm). The pre-edge and after-peak images were obtained at energy shifts of 815, 855, 995 and 1040 eV. The Ce post-edge images were obtained 899 eV. The EFTEM images were acquired at a beam dose rate of ~ 1.8 X 10^{-4} PA/nm^2 and the total beam dose for the acquisition was ~ 1.9 X 10^6 e^-/ nm^2.

Correction for spectral contamination in EFTEM:

For the astrocyte and MIDK cells dataset, there was a chemical bleed-through due to the higher atomic number lanthanide metal sticking to regions intended to be labeled by the lower atomic number lanthanide metal only. This was probably due to incomplete blocking of the first Ln-DAB. The chemical bleed-through was subtracted out by post-processing the elemental maps by the following procedure. The spectra from the two regions were normalized to approximately the same background counts. The spectra from region 1, contained the elemental edge of the higher atomic number metal only. The spectra from region 2, contained the elemental edge from both the lower atomic

number Ln and the higher atomic number Ln (bleed-through). The relative percentage of the higher atomic number Ln in spectra 2 compared to spectra 1 was calculated by integrating the signal counts for the edge in the two spectra. To ensure that the contribution from only the edge was counted, a small 10 eV background window was positioned, such that the base between the 2 peaks of the edge was at the background subtracted zero. This relative percentage or bleed-through was ~ 25 % and 45 % for the astrocyte and MDCK samples respectively. The bleed-through in spectra 2 was removed by subtracting it from spectra 1 corrected for the relative percentage. It should be noted that the spectra of higher atomic number metal in spectra 2 is a convolution of its edge with the energy-loss near edge structure and extended energy-loss fine structure of the lower atomic number edge, which tends to make the width of the elemental edge broader as compared with spectra 1. Therefore, the corrected spectra may show regions of uneven slope. A similar bleed-through subtraction was applied to the EFTEM elemental maps. For the astrocyte example, the bleed-through subtraction of the elemental maps was fairly uniform. However, for the MDCK cells example, the bleed-through subtraction led to some pixels being over subtracted and having negative values, which were set to zero.